Volume 13
Number 43
21 November 2025
Pages 21677–22046

Journal of Materials Chemistry C

Materials for optical, magnetic and electronic devices

rsc.li/materials-c

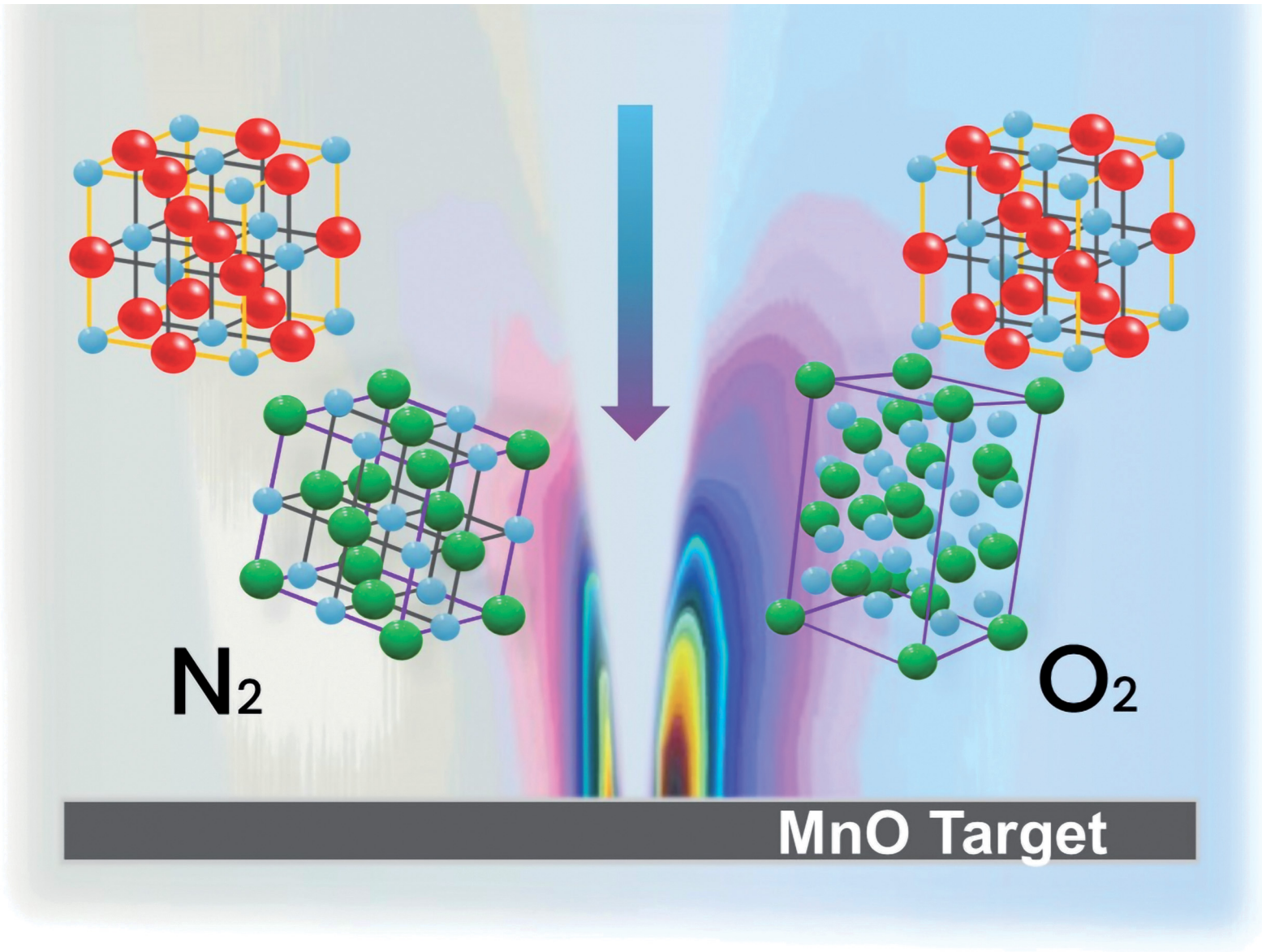

ISSN 2050-7526

ROYAL SOCIETY OF CHEMISTRY

PAPER

Stefan Andrei Irimiciuc *et al.*

The role of the N_2 atmosphere in the epitaxial growth of MnO *via* pulsed laser deposition

Journal of Materials Chemistry C

ROYAL SOCIETY OF CHEMISTRY

PAPER

View Article Online
View Journal | View Issue

Cite this: J. Mater. Chem. C, 2025, 13, 21708

The role of the N_2 atmosphere in the epitaxial growth of MnO *via* pulsed laser deposition

Stefan Andrei Irimiciuc, *[ab] Sergei Chertopalov, [a] Veronica Goian, [a] Esther de Prado, [a] Martin Vondráček, [a] Eva Marešová, [a] Petr Svora, [a] Ladislav Fekete, [a] Mariana Klementová, [a] Stanislav Kamba [a] and Ján Lančok [a]

Received 20th August 2025,
Accepted 8th October 2025

DOI: 10.1039/d5tc03142g

rsc.li/materials-c

The role of ambient gas in the epitaxial growth of manganese oxides on MgO by pulsed laser deposition was investigated by performing complex morphological and structural characterization of thin films while simultaneously monitoring the growth process with electrical probes. The growth in N_2 atmospheres leads to the formation of highly oriented MnO coatings that present compressive in-line stress and contain highly oriented defects, which are induced during growth by the high kinetic energy of the plasma. The presence of O_2 during unlocks the growth of highly crystalline Mn_3O_4 rotated by 45 deg to MgO, with X-ray photoelectron spectroscopy (XPS) measurements showing the contribution of the MnO bonding states on the surface on Mn_3O_4 due to ambient contamination of the sample. The ability of each atmosphere to promote the growth of two selected oxide phases was shown by both ellipsometry and infrared spectroscopy measurements. The *in situ* monitoring of growth highlights the ion acceleration caused by the use of N_2 compared with O_2 and the formation of a plasma environment that is optimal for the formation of molecular species as well as a strong oxide contribution to growth.

1. Introduction

Recent advancements in thin film deposition based on plasma technologies have shown that transitioning toward automated or AI-controlled processes can only occur *via* plasma diagnostic techniques implemented for thin film growth control. At the forefront of this innovative approach is the pulsed laser deposition technique (PLD).[1] PLD is renowned for its efficiency in quickly exploring the thin film growth of materials with intricate compositions spanning 2D materials,[2,3] to oxides[4,5] and even nitrides.[6–8] The technique[9] involves a complex series of processes spanning from melting and evaporation of a solid target to the formation of a highly energetic transient plasma that deposits a submonolayer of the vaporized material onto a substrate, ideally preserving the target's stoichiometry. The laser-produced plasma contains ions, electrons, atoms, molecules, and even clusters with energies that can exceed hundreds of eV or even keV. This high energy can either erode the developing layer or create metastable material phases through subplantation. Control over plasma kinetics is usually achieved by introducing a background gas that can be effectively reduce the kinetic energy to less than 1 eV *via* collisional processes.[10–13] The introduction of reactive gas in the chamber induces a complex gas phase chemical reaction that can affect both the kinetics and structure of the plasma.[14,15] This moderation is achievable with simple monitoring *in situ* diagnostic tools, such as Langmuir probes (LP),[16,17] space- and time-resolved optical emission spectroscopy[18–20] coupled with ICCD fast camera imaging[21] or mass spectrometry.[22,23] Our group recently demonstrated the excellent flexibility of Langmuir probes for *in situ* monitoring of several oxide[24,25] and halide[26] systems *via* nonbias measurements and angle-resolved measurements.

A special class of coatings that were reportedly manufactured with great success *via* PLD are based on manganese oxides.[27–29] A wide range of reported manganese oxide films have been proposed for applications ranging from lithium-ion batteries[30] to aqueous flow batteries,[31] oxygen evolution electrocatalysts[29] or thermochemical water splitting.[32] The key characteristics that make manganese oxides essential for these applications are their oxidation states and diverse polymorphisms, which also pose an important challenge in predicting the phase that will form under specific processing conditions. Studies on PLD growth of manganese oxides have explored limited regions of the phase space. Films from a MnO target formed Mn_2O_3 at 550–700 °C and Mn_3O_4 at 700–850 °C under 1–10 Pa O_2, differing quantitatively from bulk phase diagrams.[33] Reports on routes or Mn_xO_y phase formation from a Mn target at substrate temperature of 600 °C yielded Mn_2O_3 at 1 Pa, Mn_3O_4 at 10 Pa, and MnO in vacuum (10^{-3} Pa).[34] Deposition from MnO_2 at 10 Pa produced MnO_2 phases at

[a] Institute of Physics of the Czech Academy of Sciences, Na Slovance 1999/2, Prague, Czech Republic. E-mail: irimiciuc@fzu.cz
[b] National Institute for Laser, Plasma and Radiation Physics – NILPRP, 409 Atomistilor Street, Bucharest, Romania

300–450 °C and Mn_2O_3 at 550–650 °C. Mn and Mn_3O_4 targets ablated at 200–700 °C and 10^{-5}–50 Pa formed Mn_2O_3 and/or Mn_3O_4. Sputtering studies similarly showed that temperature, oxygen pressure, and morphology critically control oxidation state and performance.[28] Additionally, to reach epitaxial growth of various Mn_xO_y phases, other techniques have shown great promise such as atomic layer deposition (ALD)[35,36] with a wide range of strategies to obtain epitaxial growth such as target phase tailoring[33,37] or introduction of intermediary Pd layers.[38]

Our work focused on investigating the role of N_2 and O_2 atmospheres in the deposition of MnO thin films by pulsed laser deposition. Structural and morphological characterization of the films revealed preferential growth of the epitaxial MnO phase in N_2 and Mn_3O_4 in an O_2 atmosphere. The deposition was monitored by an angle- and time-resolved Langmuir probe. The background gas nature affects the kinetic energies of the ions as well as the structure of the time-of-arrival currents. Features of oxidation are observed throughout the measurements, with clear enhancement in plasma kinetics in the case of N_2, which acts as an accelerating medium for the MnO plasma.

2. Materials and methods

A 6 mm thick MnO target was placed inside a reaction chamber and irradiated with a YAG laser (λ = 266 nm, energy = 60 mJ, repetition rate = 10 Hz, number of pulses = 6000) at a fluence of 2.2 J cm^{-2}. The MnO target was continuously rotated to provide a fresh surface for each shot and to avoid local heating and crater formation. The target-to-substrate and LP distances were 50 mm and 37 mm, respectively. The plasma investigations were performed under a residual vacuum of 1×10^{-4} Pa and at 5×10^{-2}, 5×10^{-1}, 2, 5, and 10 Pa O_2 and N_2 atmospheres. A cleaning procedure of the target was employed before each experiment to remove any surface contamination of the target by irradiating the target during 1200 pulses at 2.2 J cm^{-2} (for other details on the setup geometry and overall description of the LP technique, please see[39]). The measurement circuit is the classical circuit, as previously reported.[40] The signal from the tungsten LP (diameter of 0.2 mm and exposed length of 2 mm) was collected across a load resistor (1.2 kΩ) with a Tektronix DPO 4140 oscilloscope. All electrical measurements were synchronized by a fast silicon photodiode (Thorlabs FDS100) placed outside the chamber.

Mn_xO_y thin films were deposited on MgO (100) substrates positioned 50 mm from the target *via* 6000 consecutive pulses at 650 °C under identical irradiation conditions at selected O_2 and N_2 pressures. The transmittance spectra of the resulting films were measured by a spectrometer (USB4000, Ocean Optics) in the spectral range from 300 to 890 nm. The light source (DT-mini-2-GS, Ocean Optics) was coupled with a focusing lens by an optical fiber with a 200 μm core diameter. The light spot diameter on the sample was approximately 2 mm, which determined the lateral resolution of the transmittance measurement. AFM (AFM Dimension ICON, Bruker) was used to investigate the surface morphology, roughness and thin film thickness. The measurements were performed under ambient conditions, and images were obtained in peak force tapping mode using ScanAsystAir tips with a scan area of 1×1 μm^2.

X-Ray diffraction (XRD) measurements were performed using three different diffractometers. The samples were examined with an X-ray diffractometer (Empyrean, Malvern Panalytical) with monochromated Cu K_α radiation (wavelength λ = 1.54151 Å, U = 45 kV, I = 30 mA) in grazing incidence XRD mode. The incident angle was 0.85°, which corresponds to ~10 mm of sample irradiation. The XRD measurements were made at the central part of the deposited film with an area of 10×10 mm^2. High-resolution XRD (HRXRD) measurements were carried out *via* a SmartLab SE Multipurpose diffractometer (Rigaku Corp., Tokyo, Japan) with Cu $K\alpha_1$ radiation. The incident beam optics included a parabolic Göbel mirror and a two-bounce Ge (220) monochromator. For the diffracted beam, a 2.5° Soller slit and a HyPix-3000 2D detector operating in 0D mode were utilized. Finally, pole figures were obtained *via* an X'Pert Pro PANalytical diffractometer (PANalytical B.V., Almelo, Netherlands) with Co Kα radiation, which was configured with a point-focus X-ray source and an X'Celerator detector.

The composition of the films was investigated *via* an XPS NanoESCA Omicron Nanotechnology instrument. Monochromatic Al anode K_α radiation (E = 1486.7 eV) was used as an X-ray source. The analyzed spot size was 100×300 μm^2, and several positions on the sample were probed. For depth profiling, Ar^+ sputtering was performed at 2×10^{-4} Pa, an accelerating voltage of 3 keV and an ion incidence angle of 15° with respect to the sample surface normal. One-minute depth profiling removed approximately 0.5/1 nm of the thickness of the material. Spectral fitting was conducted *via* CasaXPS software. Measurements were performed in a mode with 0.5 eV energy resolution.

Transmission electron microscopy (TEM) was carried out on an FEI Tecnai TF20 X-twin microscope operated at 200 kV (FEG, 2.5 Å point resolution) equipped with an EDAX energy dispersive X-ray (EDX) detector (30 mm^2, 135 eV resolution) and a Gatan imaging filter (GIF) Quantum for electron energy loss spectroscopy (EELS). The microscope was also used in scanning mode (STEM) with a high-angle annular dark field detector (HAADF). TEM images, selected-area electron diffraction (SAED) patterns, and EELS spectra were recorded on a Gatan UltraScan CCD camera *via* the Digital Micrograph software package. SAED patterns were evaluated *via* CrysTBox software. The EELS data were collected in STEM mode with a 5 mrad convergence angle, a 10 mrad collection angle, and an energy resolution of 1.2 eV. EELS quantification was performed *via* the Digital Micrograph software package. Lamellas for the TEM observations were prepared *via* the focused-ion beam technique using an FEI Quanta 3D with a Ga source.

IR reflectivity spectra were obtained at room temperature using a Fourier transform IR spectrometer Bruker IFS 113v in the frequency range of 30–3000 cm^{-1}. Reflectance measurements were performed in near-normal incidence geometry. In the far and middle IR frequency ranges, two deuterated triglycine sulfate detectors were used.

3. Results and discussion

3.1 Thin film investigations

The plasma diagnostics revealed that for the deposition of MnO, one can define specific pressure ranges where the properties suffer significant changes. These pressure regimes are consistent with the mean free path values, with changes of 3 orders of magnitude in the 10^{-2}–10 Pa range of O_2 and N_2. The results for the thin films deposited at 10^{-2}, 10^{-1}, 2 and 10 Pa on MgO (001) substrates heated to 650 °C are discussed below. In Fig. 1, the AFM images of the deposited coatings are presented. A detailed representation of the AFM images for other growth conditions is given in Fig. S1. Under low-pressure conditions (10^{-2} and 10^{-1} Pa), the films deposited in N_2 have a similar morphology, with 100 nm large cubic crystals and an average roughness of 50 nm, whereas under O_2, a similar morphology is observed, with smaller crystals and a roughness of 2 nm. The subsequent increase in N_2 pressure results in a fractal-like morphology and a 1–2 nm roughness. The addition of O_2 led to the formation of larger crystals with an average roughness of 16 nm. Thus, in both atmospheres, the size of the crystals can be tailored by adjusting the ion kinetic energy during deposition. The transition in morphology at 2 Pa is consistent with the change in the dominant ionic structure.

For the films deposited in N_2 atmospheres, the transparency regime is indicated by film thickness interferences with average transmittance (350–900 nm) of 70–80%, whereas coatings deposited in high-pressure O_2 have a reduced transmission of approximately 10% (Fig. 2(a)). By implementing the Tauc plot method, the direct band gaps were estimated. For the N_2 case, the band gap increases in the 3.9–4.33 eV range with increasing N_2 pressure from 10^{-2} to 10 Pa, whereas for the O_2 case, it increases from 1.1–1.9 eV in the same pressure range. It is clear that a N_2 atmosphere generates a MnO phase, whereas O_2 generates a Mn_3O_4 phase with specific defects. According to,[41,42] band gap values above 4 eV are induced by O vacancies, which implies the following reaction: $O_O^{\times} \rightarrow V_O^{\bullet\bullet} + 2e' + \frac{1}{2}O_2(g)$. This is understandable for our deposition conditions, as the N_2 atmosphere limits O_2 inclusion in the MnO films. For the films deposited in an O_2 atmosphere, the band gap value implies the presence of Mn vacancies with two associated electrons.

Ellipsometry measurements were used to determine the optical constants (n and k) and optical band gap (E_g) of thin layers of MnO and Mn_3O_4. The optical model used to characterize the samples consists of a MgO substrate, a MnO/Mn_3O_4 thin layer and surface roughness. This model best defines the structure of the samples, as it provides the best fit. It can be seen from Fig. 2(b) that the thin films of MnO and Mn_3O_4 are transparent over some part of the measured spectral range (MnO $\lambda > 650$ nm, Mn_3O_4 $\lambda > 350$ nm). This was used as a starting point for initial analysis of the approximate values of the refractive index and thickness (Cauchy model). For comparison, the thickness of the layers was measured on a KLA Tencor profilometer (between 180 nm and 200 nm depending on the growth conditions, more details are given in Fig. S2 and S3). The measured values were consistent with the optical data. To describe optical dispersion over a wide wavelength range, the model was improved by including 1 Tauc–Lorentz oscillator and 1 Gaussian oscillator. The optical band gap (E_g) was determined from the Tauc–Lorentz formula, which was found to be E_g(MnO) = 4.0 and E_g(Mn_3O_4) = 1.9. The optical constants n and k of the MnO and Mn_3O_4 thin layers derived from SE analysis are presented in Fig. 2(b).

Accurate MnO phase identification can be rather difficult because of the large number of available oxidation states.[43] Kerisit *et al.* provide a comprehensive empirical path to phase differentiation. The shape of the Mn 2p peak is similar to that reported by,[28,36] who investigated the influence of the nature of MnO (island, film, bulk) on the shape and structure of the Mn 2p peak. By following the fitting procedure for Mn 2p,[43] a 5 peak deconvolution was used (Fig. 3(b)), which first tentatively confirms the presence of the MnO phase. The possible oxidation states available can be identified from the presence of high-BE satellites in the 2p region, such as those indicated in Fig. 3(a). These satellites are unique identifying features of the Mn 2p peak and are positioned at a 6.15 eV higher binding energy. These findings are in good agreement with the Mn 2p core level spectra reported in the literature for MnO(001) films.[33] Moreover, the multiplet splitting energy (Δ) of the Mn

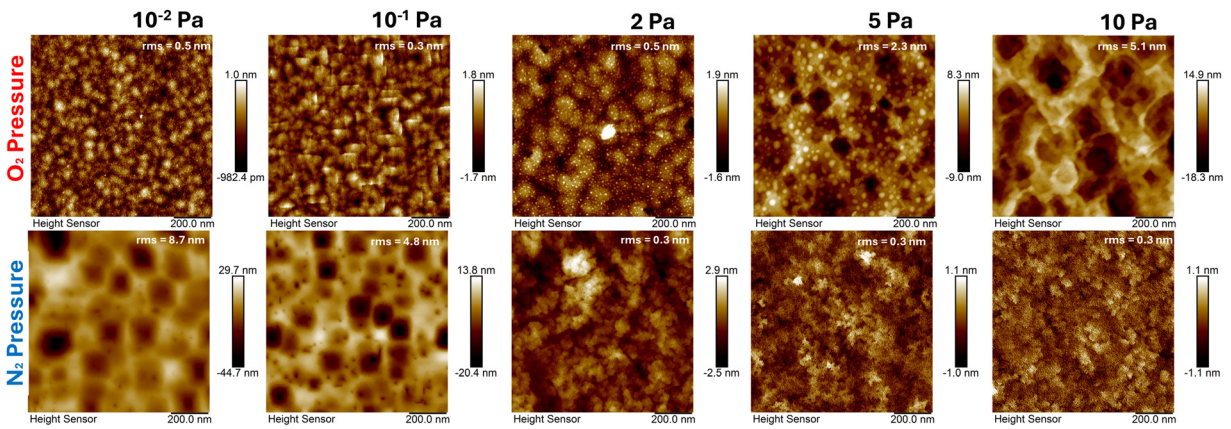

Fig. 1 AFM images of the MnO thin films deposited in various N_2 and O_2 pressures.

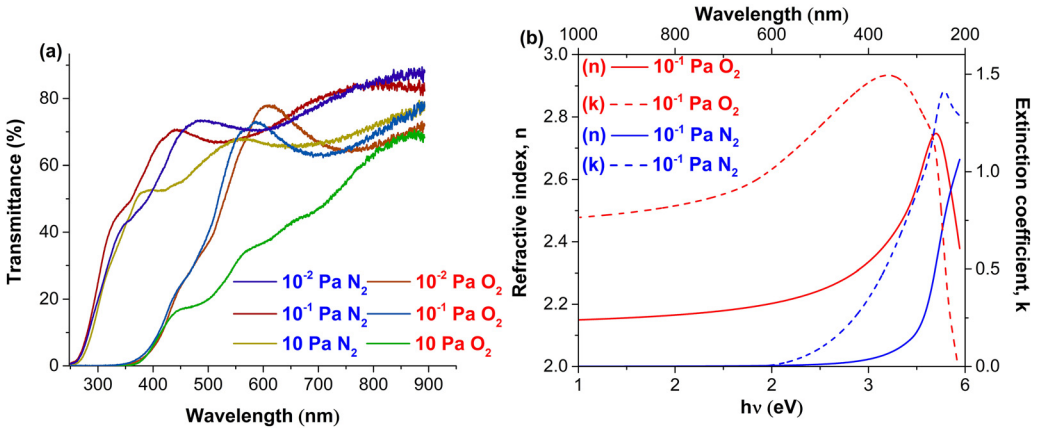

Fig. 2 Transmittance spectra of MnO films (a) and ellipsometry data (b) (refractive index and extinction coefficient).

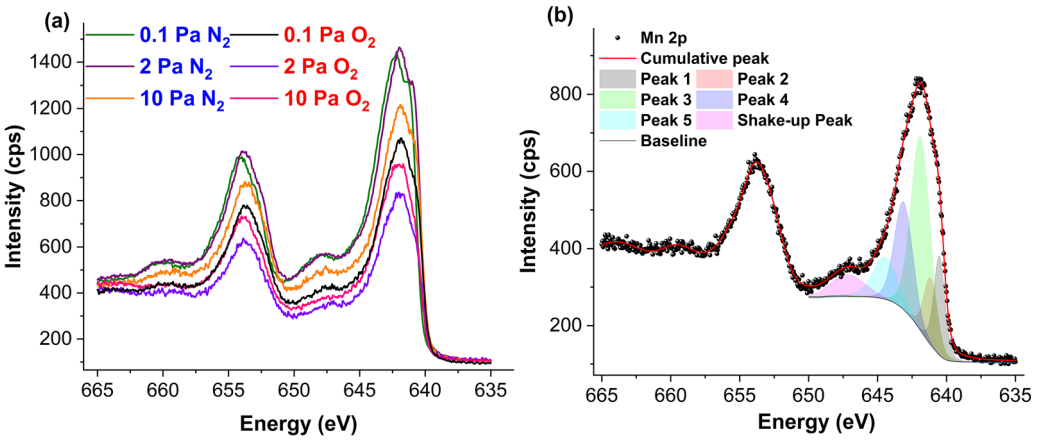

Fig. 3 XPS spectra of Mn2p for various deposition conditions (a) and the 5 peak fit characteristics for MnO (b).

3s peak can be used as a quantitative indicator of the Mn oxidation state: MnO (6.1 eV), Mn_3O_4 (5.7 eV), Mn_2O_3 (5.4 eV), and MnO_2 (4.4 eV); however, overlap of the Mn 3s and Mg 2s peaks necessitates deconvolution for MnO_x thin films on MgO. The observed multiplet splitting (Fig. S4b) for the N_2 case is approximately 5.7 eV, whereas for the O_2 case, 6.1 eV is consistent with bulk MnO, and the area ratio of the parallel (low-energy) and antiparallel (high-energy) Mn 3s peaks is ~1.6, which is slightly above the predicted value of 1.4. This result implies the preferential formation of the MnO phase in the samples grown in a N_2 atmosphere, whereas the samples grown in O_2 have a smaller energy split characteristic of the formation of Mn_3O_4. Moreover, there is a 2 : 1 peak area ratio in the 3s XPS spectra of paramagnetic 3d transition metals arises from many-body effects beyond simple exchange interaction, which create two final states from the interaction between the core hole and the unpaired valence electrons. The observed 2 : 1 intensity distribution reflects the statistical degeneracy of these multi-electron states, with the lower energy peak often having a higher intensity due to these complex atomic and electronic correlation effects. This conclusion is confirmed by the data presented in Fig. S4(a) and (b), where it can be seen that MnO satellites are present only in the as-received samples deposited in a N_2 atmosphere. The results are in good agreement with the optical transmission and ellipsometry investigations previously discussed.

The samples deposited at 0.1 Pa O_2 and 0.1 Pa N_2 were selected for further analysis because of their similar dynamic deposition regimes. Fig. 4(a) shows the symmetric ω–2θ scans on a quadratic scale for the selected samples, with the vertical axis truncated for better visualization due to the extremely high intensity of the substrate. Both films are oriented out-of-plane in the same direction as the substrate and exhibit a unique phase, cubic MnO for deposition in a N_2 atmosphere or tetragonal Mn_3O_4 in the case of O_2. Two key observations can be highlighted: the diffraction peaks of MnO are asymmetric on the right side, a phenomenon related to defects, as indicated by transmission measurements. On the other hand, a greater width of the diffraction peaks can be observed in the case of Mn_3O_4, indicating a higher microstrain, along with a notably lower intensity. The crystalline quality of the layer, understood as the out-of-plane misorientation, was explored through rocking curve (ω scan) measurements of the symmetric 002 reflection. The results are shown in Fig. 4(b). MnO exhibited a full

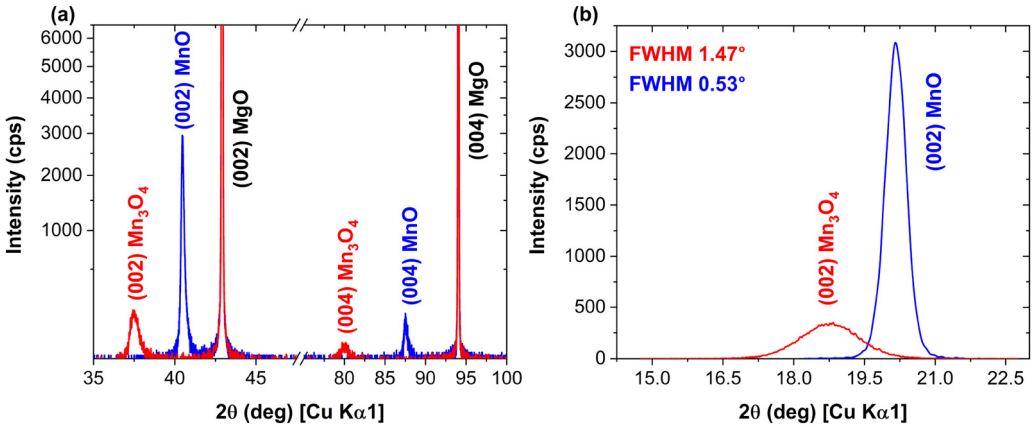

Fig. 4 HRXRD measurements as a function of the growth atmosphere: (a) ω–2θ scans and (b) rocking curves. The peaks are indexed according to their phase and (*hkl*). The vertical axis in Fig. 4(a) is truncated for better visualization.

width at half maximum (FWHM) of approximately 0.5°, indicating good crystalline quality; in contrast, Mn_3O_4 showed a significantly larger FWHM, reflecting lower quality.

The texture of the samples was examined through pole figure measurements, with the results on a logarithmic scale shown in Fig. 5. Pole figures for the (002), (022), and (111) reflections of MnO are presented in Fig. 5(a)–(c), respectively. No additional spots beyond those expected for a cubic structure are observed: one pole for the symmetric (002) reflection and four poles spaced azimuthally 90° apart at $\chi \approx 45°$ for the (022) reflection and at $\chi \approx 54.74°$ for the (111) reflection. Similarly, no additional features are observed in the pole figures for the Mn_3O_4 layer, corresponding to the (004), (033), and (224) reflections, as shown in Fig. 5(c)–(e), respectively. The additional spots visible in these figures are due to the tails of various diffraction peaks from MgO.

From the results shown above, we can conclude that the films grow epitaxially and without twins. In the case of MnO, the growth occurs as cubes on cubes, whereas the Mn_3O_4 layer grows with its lattice 45° azimuthally rotated relative to the substrate. Therefore, the epitaxial relationships are as follows:

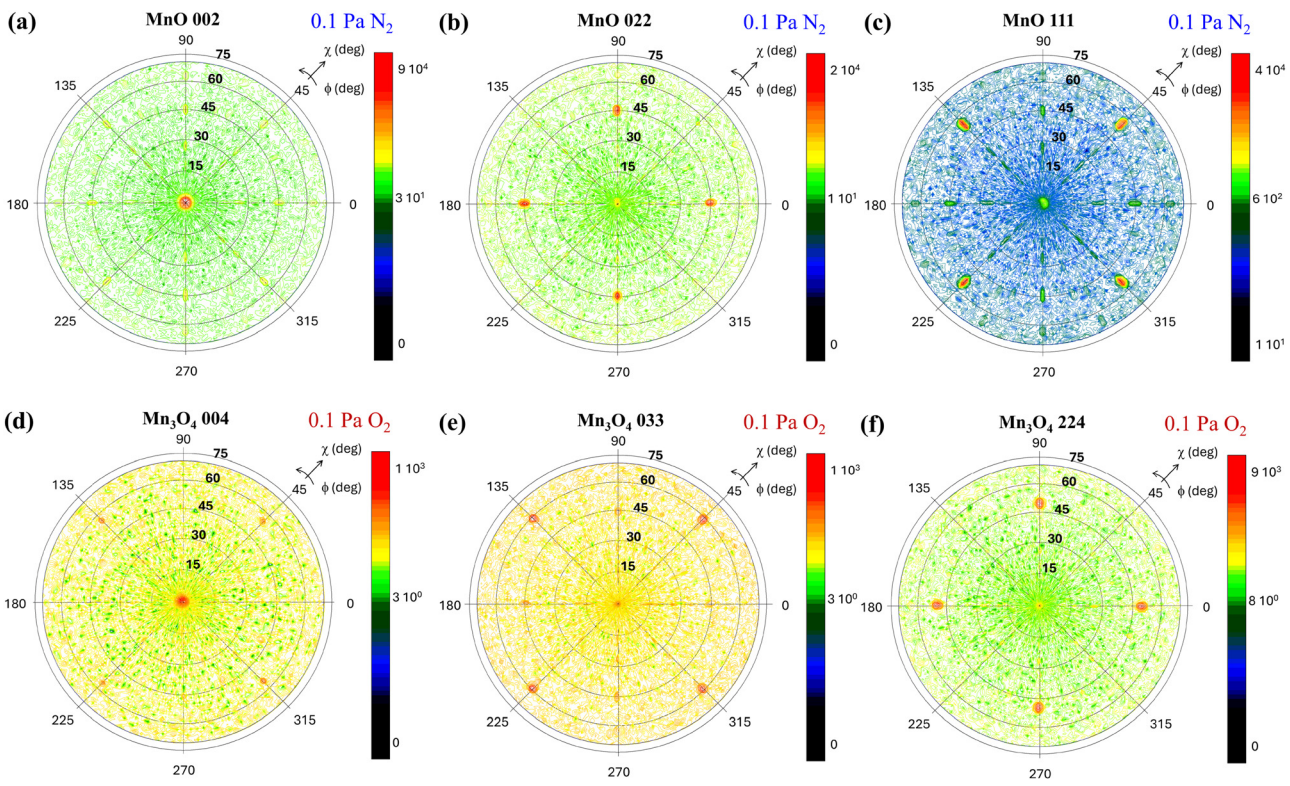

Fig. 5 XRD pole figures of the films: (a)–(c) MnO and (d)–(f) Mn_3O_4.

$$(001)_{MnO}||(001)_{MgO},\quad [100]_{MnO}||[100]_{MgO}$$

$$(001)_{Mn_3O_4}||(001)_{MgO},\quad [100]_{Mn_3O_4}||[110]_{MgO}$$

The in-plane *a*- and out-of-plane *c*-lattice parameters were determined from reciprocal space maps (RSMs). Fig. 6(a) and (b) display the (002) symmetric and (024) asymmetric RSMs for the MnO layer, respectively. Upon visual inspection of the asymmetric RSM, it is evident that the layer is very relaxed. The (002) symmetric RSM for the Mn_3O_4 layer is shown in Fig. 6(c), and the asymmetric (228) RSM is shown in Fig. 6(d). Owing to the rotation of the lattice, the relaxation state of the Mn_3O_4 layer cannot be inferred from the asymmetric RSM, as the corresponding (228) reciprocal space point of the substrate appears at a different azimuth. In the inset of this figure, a wide snapshot of the reciprocal space is shown, where the (204) reflection of the substrate is visible, confirming the accuracy of the measurement.

In the case of MnO, the lattice mismatch imposed by the substrate (approximately 5%) induces a biaxial stress that modifies the structure of the film. As a consequence, a compressive in-plane strain is present. The calculated in-plane *a*- and out-of-plane *c*-lattice parameters, along with the corresponding tabulated values and the resulting strains, are summarized in Table 1.

Lamellas from two samples (0.1 Pa N_2 and 0.1 Pa O_2) were studied in detail *via* TEM methods: imaging (including HRTEM), electron diffraction (Fig. 7) and spectroscopy (Fig. 8).

Table 1 Calculated in-plane (*a*) and out-of-plane (*c*) lattice parameters of MnO and Mn_3O_4 thin films compared with tabulated bulk values. The corresponding in-plane and out-of-plane strain values are also included

Sample ID	Phase	*a* (Å)	*c* (Å)	*e* (%) in-plane	*e* (%) out-of-plane
0.1 Pa N_2	MnO	4.433	4.455	−0.29	0.20
PDF 04-005-4310	MnO	4.446			
0.1 Pa O_2	Mn_3O_4	5.704	9.585	−0.30	−0.25
PDF-04-007-1841	Mn_3O_4	5.765	9.442		

The overall appearance of the two samples is quite different (Fig. S5). The N_2 sample shows strong contrast variations that might signify strain or other changes in the structure, such as the presence of defects. In addition, the surface of a sample is not perfectly flat and displays dips and dents. In contrast, the O_2 sample has a flat surface and appears more homogeneous. The thickness of the layers differ between the two samples. The peak width was 188 nm for the N_2 sample and 245 nm for the O_2 sample.

From the SAED patterns (Fig. 7), the structures of both the layer and the substrate were investigated, as were their mutual growth relationships. In the layer of the N_2 sample, all high-intensity diffraction spots correspond well to cubic MnO. However, there are additional low-intensity diffraction spots present in the positions of reflections (110), (310), *etc.*, which violate the extinction rules for F-centering in cubic MnO. To explain the presence of these spots, we also tested matching the

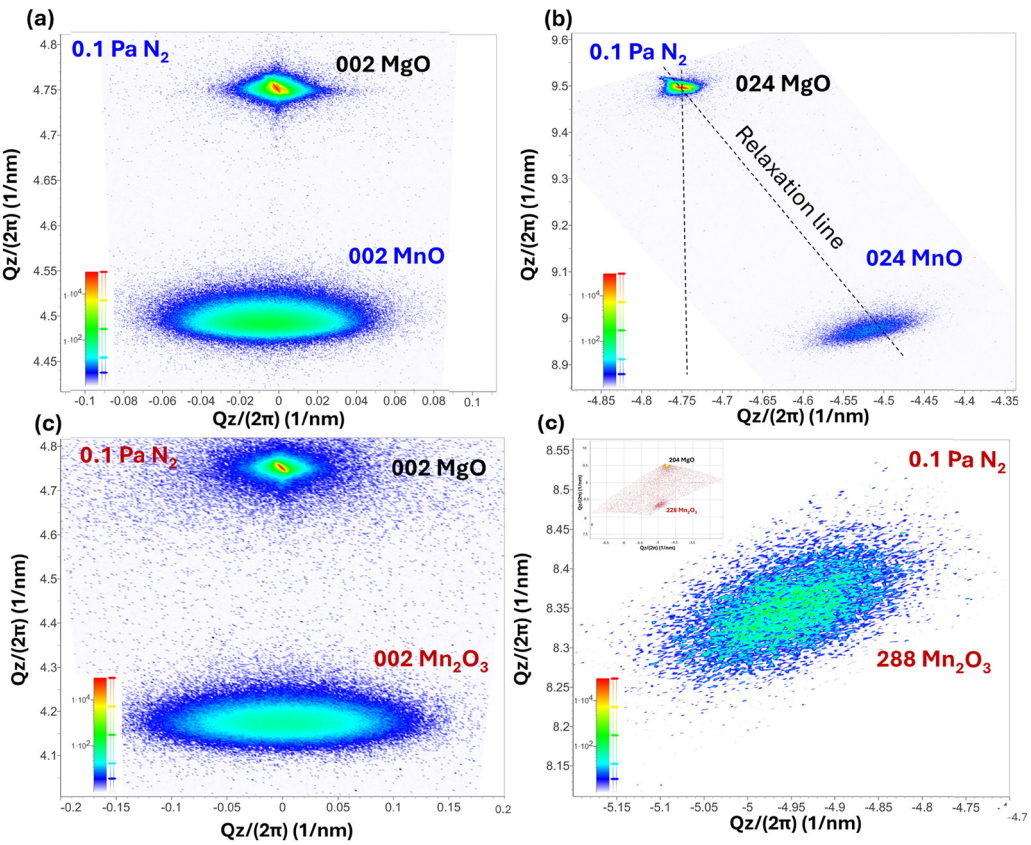

Fig. 6 Symmetric (a) and (c) and asymmetric (b) and (d) reciprocal space maps of the films: MnO (a) and (b) and Mn_3O_4 (c) and (d).

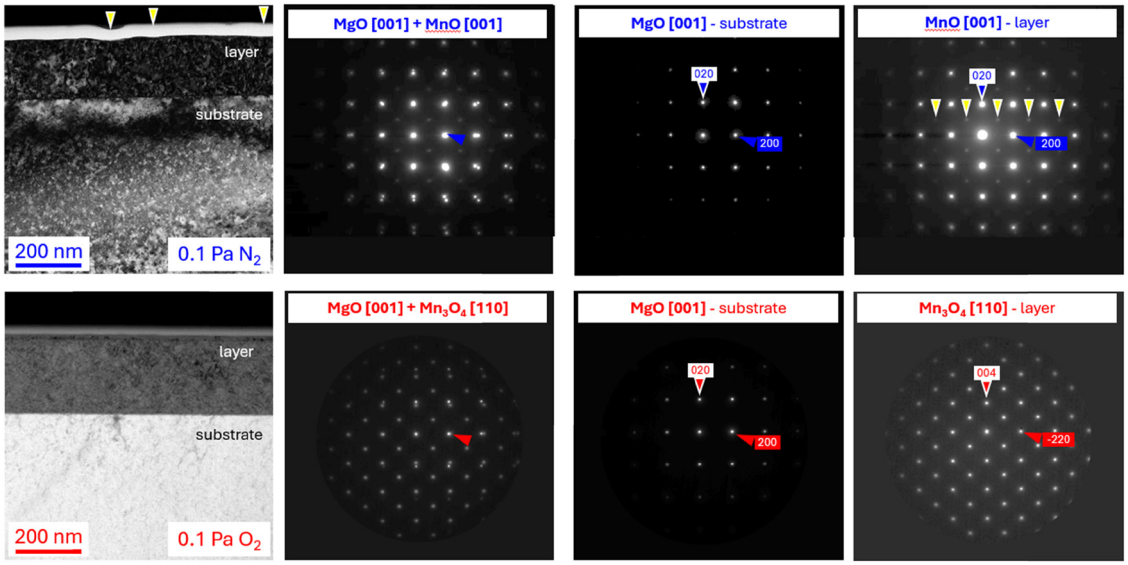

Fig. 7 TEM images of samples prepared in N_2 and O_2 atmospheres. The top row shows measurements from samples prepared in N_2. The layer is formed by MnO with a cube-to-cube growth relationship to the MgO substrate: MgO(001)||MnO[001], MgO(200)||MnO(200). The yellow arrows highlight additional diffraction spots, which are inconsistent with cubic MnO and are most likely caused by defects in the structure. The bottom row shows measurements from samples prepared in O_2. The layer is formed by tetragonal Mn_3O_4 with the growth relationship rotated by 45 deg to the MgO substrate: MgO(001)||MnO(110), MgO(200)||Mn_3O_4(−220).

experimental SAED patterns against simulated tetragonal Mn_3O_4 diffraction patterns (Fig. S6). We were able to reproduce the additional spots; nevertheless, to match, the unit-cell parameters had to be reduced by 9%, which is too much even for electron diffraction.

Bright-field and dark-field (made with 110 diffraction spots) images highlight inhomogeneities in the layer (Fig. 8). Cone structures with the base connected to the interface with the MgO substrate and narrowing as layer growth progresses are displayed. These structures are composed of defects perpendicular to the (110) direction in MnO, which cause partial loss of periodicity and appear as extinction-violation diffraction spots in the SAED patterns. They reflect the misfit of the MgO substrate and the MnO layer at the initial state of growth, which later relaxes as the layer grows into the more periodic structure. This is documented by the FFTs of the HRTEM image (Fig. S7), where the FFT spots from MgO and well-ordered MnO (area 1) are sharp, whereas the FFT spots from area 2

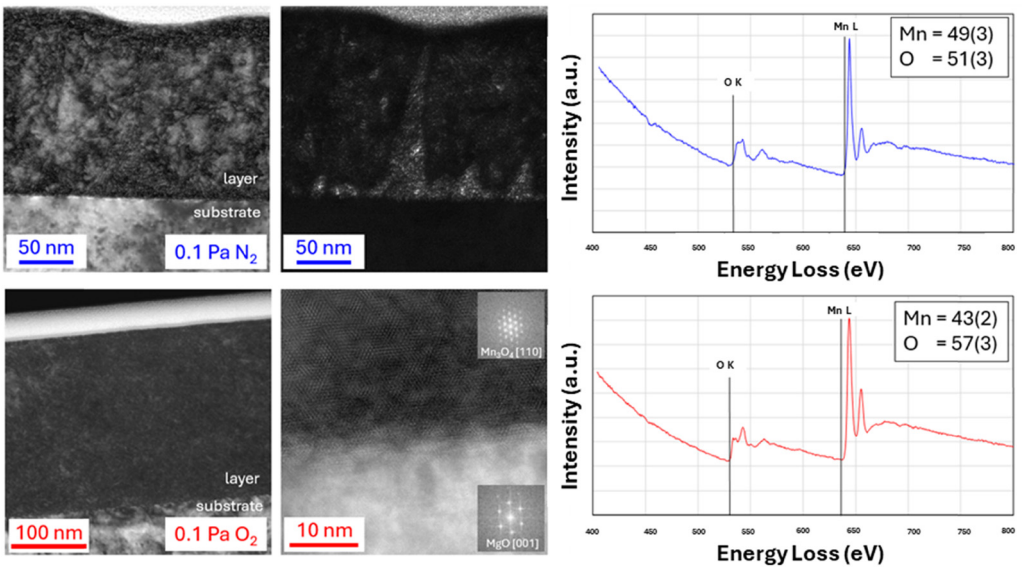

Fig. 8 TEM images of samples prepared in N_2 and O_2 atmospheres. The top row shows measurements from samples prepared in N_2. Bright-field and dark-field (made with 110 diffraction spots) images highlight inhomogeneities in the layer. The EEL spectrum shows a composition corresponding to MnO. The bottom row shows measurements from samples prepared in O_2. The layer is homogeneous, and the EEL spectrum corresponds to Mn_3O_4.

containing many defects diffuse, reflecting the partial loss of periodicity.

The chemical composition of the layers was studied *via* EDX and EELS. The main reason was the uncertainty in the phase composition of the layer in the N_2 sample. Mn-oxides exist in several forms: MnO (50/50 ratio), Mn_3O_4 (43/57 ratio) and Mn_2O_3 (40/60 ratio). The EDX profiles (Fig. S8) show a homogeneous distribution across the layer but yield unrealistic compositions for Mn-oxides, *e.g.*, Mn/O ratios of 30/70 for Mn_3O_4 and 40/60 for MnO, whereas the composition of MgO corresponds to the perfect 50/50 ratio. This is caused by strong MnL/OK peak overlap in the EDX data (OK – 0.525 keV, MnL – 0.556 keV, 0.637 keV). Therefore, EELS was employed to obtain the correct results (Fig. S9). In EELS, the edges are well separated (OK – 532 eV, MnL1 – 651 eV, MnL – 640 eV). Indeed, the EEL spectra give composition ratios close to the expected values of 49(3)/51(3) for MnO and 43(2)/57(3) for Mn_3O_4 (Fig. 8). In addition, we searched for some variations between the perfect MnO and defective MnO in the N_2 sample, but no such variation was detected, as shown in the profile in Fig. S7.

The layer of the O_2 sample is formed by tetragonal Mn_3O_4 with the growth relationship rotated by 45 deg to the MgO substrate: MgO[001]||Mn_3O_4[110], MgO(200)||Mn_3O_4(−220) (Fig. 8). The layer is homogeneous, and the chemical composition according to the EEL spectrum corresponds to Mn_3O_4 (Fig. 8).

The IR reflectance spectra of thin films prepared in various O_2 and N_2 atmospheres with different partial pressures were measured, and the results are presented in Fig. 9. Notably, the IR reflectance spectra can offer fast and accurate information about the chemical composition of the thin layer because different Mn oxides have completely different selection rules for the activity of polar phonons. IR spectra are sensitive to phonons even in films with thicknesses less than 50 nm.[44] The spectra of only the films produced at 0.1 Pa of O_2 and N_2 and the bare (100) MgO substrate exhibit a broad reflection band (restrahlband) between 400 and 750 cm^{-1} (see the black curve). Since MgO crystallizes in a simple rock salt structure, it has only one IR-active phonon allowed by symmetry, which we see at ∼400 cm^{-1} [45] (the transverse optical frequency of this mode). The decrease in reflectivity at ∼750 cm^{-1} corresponds to the longitudinal phonon frequency of the same optical mode, and the weak minimum at 650 cm^{-1} appears due to multiphonon absorption. The increase in reflectivity below 100 cm^{-1} is due to reflection from the back of the 1 mm thick MgO wafer, as the substrate becomes IR transparent in this region. The IR spectrum of the thin film grown in a N_2 atmosphere (red curve) shows one additional reflective band near 274 cm^{-1}, in addition to the reflective band from MgO. This indicates that the film is MnO, since this material, like MgO, has only one IR-active optical phonon. Its frequency corresponds well to that observed in the MnO crystal.[46] Previously published IR spectra of MnO thin films on MgO show slightly different phonon frequencies because the films in[45] experienced a strain that shifted the phonon frequency in MnO.

The spectra of the films grown in an O_2 atmosphere are more complex, with three peaks below 250 cm^{-1} and two

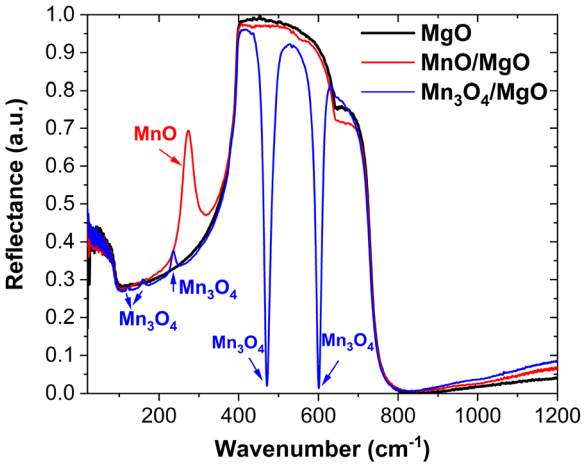

Fig. 9 Unpolarized room-temperature IR reflectance spectra of MnO (grown in N_2 atmosphere) and Mn_3O_4 (grown in O_2 atmosphere) thin films deposited on (001) MgO substrates. IR reflectance spectrum of the pure MgO substrate as a reference.

minima at 470 and 600 cm^{-1}, in addition to the MgO response. Their frequencies correspond to the phonon frequencies of the thin film. In fact, if the TO phonon frequencies of the film lie below the TO frequency of the substrate, they appear as reflection peaks in the IR spectrum. However, if the phonon frequencies of the film lie within the restrahlband of the substrate, they appear as minima in the reflection spectra.[44] From the number of phonons in the thin film, it is clear that this layer cannot be MnO. However, the phonon frequencies correspond well to the stronger phonons in Mn_3O_4.[47]

3.2 *In situ* monitoring the deposition process

To better understand the role of the growth environment (O_2, N_2) in the formation of specific manganese oxide phases, one needs to understand the complex particularities of the growth of Mn_xO_y. In the following, the Langmuir probe (LP) method for the angle- and time-resolved approach of MnO plasma, which involves expansion in N_2 and O_2, is discussed. In Fig. 10(a) and (b), we plot the plasma current temporal traces collected from the MnO plasma during the deposition process. The currents were collected along the main expansion axis, which is defined as the axis orthogonal to the impact point on the target surface. Under vacuum conditions, the charge current is relatively small and is described by two negative peaks attributed to electron and O^+ ions (at 400 and 700 ns) and two positive peaks (at 1 μs and 10 μs) attributed to Mn^-. The peak attribution is performed on the basis of our previous work,[24] which shows that oxide plasmas generated by laser ablation of ceramic targets have a complex contribution to the ionic current with multiple ionized metal ions, ionized molecular fractions and negative O charges. The charge separation is due to the presence of multiple ionized species in the plasma coupled with the well-known plume splitting effect, which was previously reported by several groups.[48,49] The addition of O_2 leads to the presence of multiple negative peaks induced by the ionization of O species. This change in the nature of the

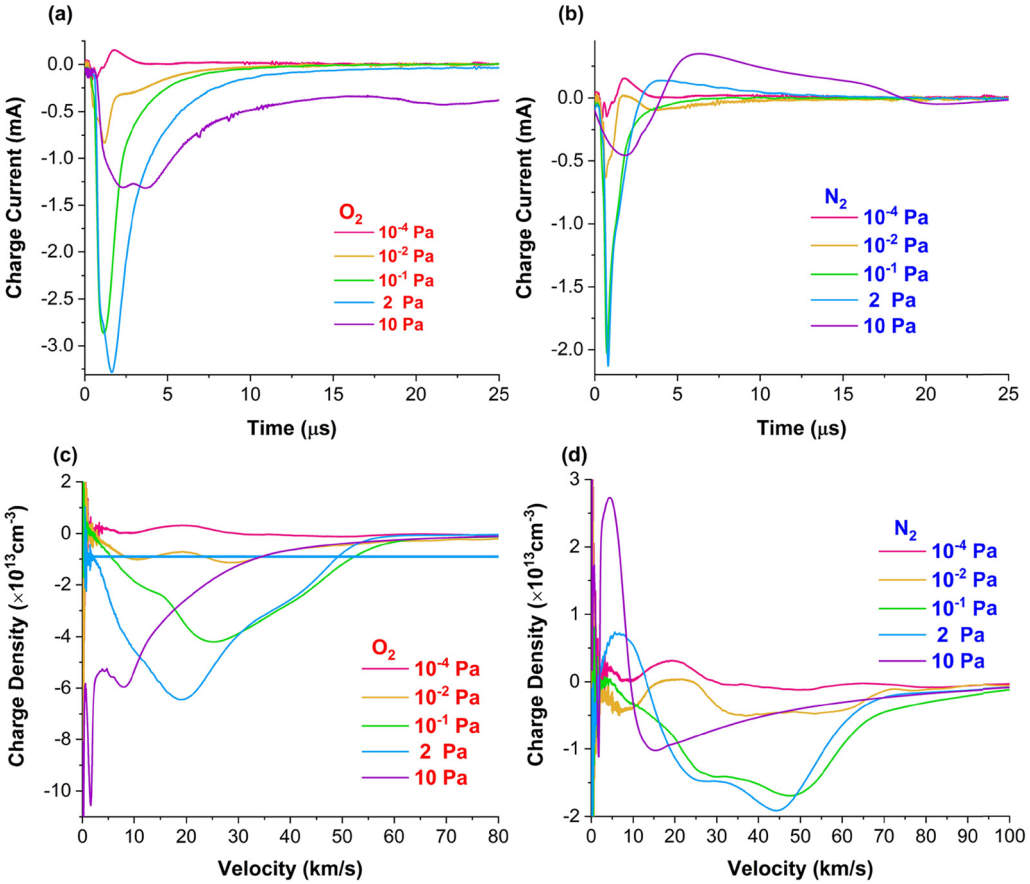

Fig. 10 Selected current charge temporal traces for MnO plasma expansion in O_2 (a) and N_2 (b) atmospheres and their respective charge density velocity distributions (c), (d).

current was also reported by our group in ref. 50. The presence of N_2 led to a similar increase in charge density, with important contributions from positive peaks above 2 Pa. This behavior can be correlated with the ionization of the N_2 working gas and a reduction in the gas phase oxidation processes during deposition. The low oxidation conditions are correlated with the lower average oxidation state found in the MnO films deposited in N_2.

In Fig. 10(b) and (c), the charge density velocity distributions are shown, according to the procedure from.[51,52] The expansion velocity of the plasma increases as the O_2 and N_2 pressures increase to 2 Pa, followed by a decrease in the high pressure region. This is due to the ionization of the working gas, which leads to the formation of an accelerating double layer in front of the plasma. The acceleration of the ions has a threshold at 2 Pa, which results in a reduction in the expansion velocity, with 11% in the N_2 case and 24% in the O_2 case. Overall, the expansion velocities derived for MnO expansion in N_2 are higher than those in O_2 by a factor of 2. This is due to the local acceleration of selected species in front of the plasma. The ionization of the N_2 atmosphere leads to the presence of N^+, which predominantly accelerates negative charges in the plasma. The deceleration of the plasma above 2 Pa coincides with a mean free path from 3.5 mm, which defines highly collisional regime movement in the PLD geometry of the reaction chamber. The ionization of working gas and understanding the subsequent role of N_2 in deposition are key aspects in explaining the phase tailoring during growth. During deposition, a N ionized cloud is generated at the front of the expanding MnO plasma; thus, the deposited film will be passivated by N_2. The subsequent pulses, owing to their higher energy, will therefore clean the adsorbed N_2 molecules from the surface, allowing the deposition of the pure MnO phase.

Using the approach from[24,50,51] in Fig. 11, we plotted pressure-angle maps of the kinetic energy of the two main ionic groups and Mn^- densities in the laser-produced plasmas. The highly kinetic ionic group is defined by energies in the 500–650 eV range in low-pressure oxygen environments of 10^{-4}–2 Pa, followed by a decrease to 70 eV in all expansion directions. The low kinetic group is defined by a multipeak structure with a first peak at 0.1 Pa O_2 and a second peak at 2 Pa and 10 Pa. The maximum values are reached above 2 Pa and are in the 30–40 eV range. On the larger expansion axis, a two-maxima distribution is observed, with the first peak at 12 eV observed at 10^{-4} Pa and the second peak at 0.1 Pa at 15 eV. A major aspect that needs underlining is the fact that the high and low kinetic groups have a complementary distribution. The low-energy kinetic group is dominant at high O_2 pressures, whereas the high-energy kinetic group is dominant at low

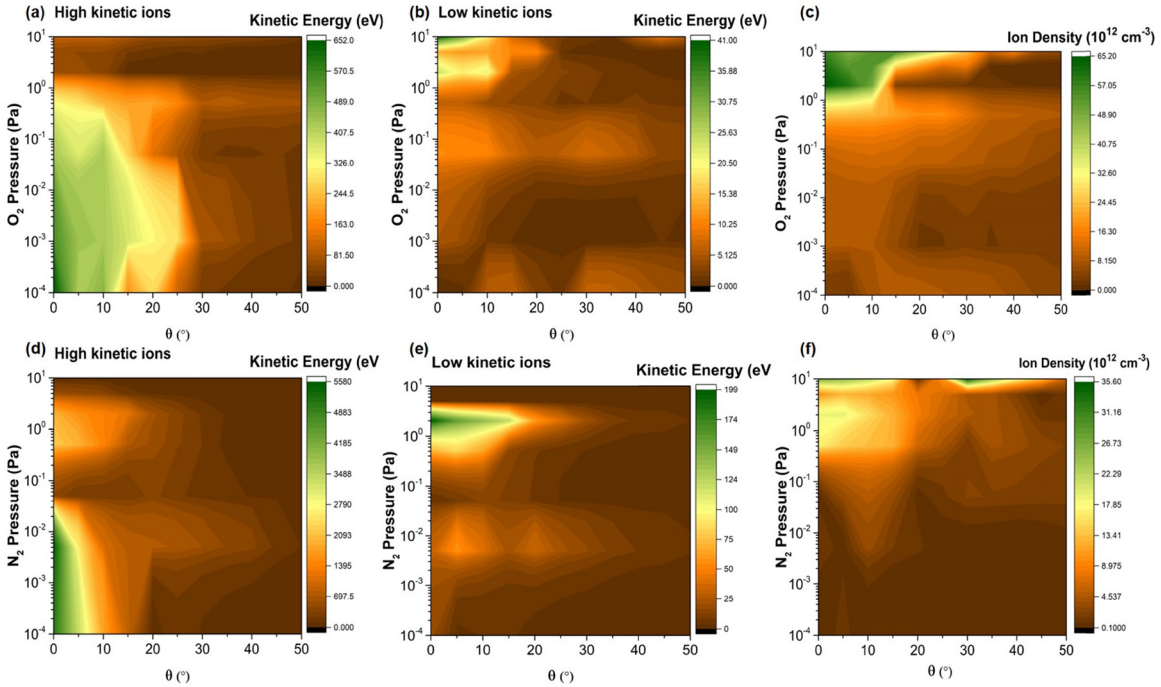

Fig. 11 Pressure and angle mapping of kinetic energy and ion density for plasma generated under various O_2 (a)–(c) and N_2 (d)–(f) conditions.

pressures. With O_2 addition above 2 Pa, strong thermalization of the plasma occurs. The thermalization process[53] involves increasing the collision rate of the ions and thus secondary ionization processes. The kinetic energy of both ionic groups is greater than the individual ionization energies of the Mn (7.34 eV) and O (13.6 eV) atoms as well as the dissociation energies of the O_2 and MnO bonds. This conclusion is supported by the quasi exponential increase in the ion density, with a maximum of 6.5×10^{13} cm^{-3} at 5 Pa.

In the N_2 case, the high kinetic energy group has a maximum (5.5 keV) at 0–5° at 10^{-4}–10^{-2} Pa and a second peak of 3 eV in the 0–20° range at 2 Pa, followed by a decrease to 500 eV at 10 Pa. The low kinetic group is described by a two-peak distribution throughout the plasma volume with a maximum of 80 eV at 10^{-2} Pa and a secondary peak at 190 eV at 2 Pa. The higher velocities derived in the N_2 case are due to the plasma front acceleration of the plasma induced by the formation of a N^- O^+ charge separation. The ion density increases with the addition of N_2, with two maxima of 1.7×10^{13} cm^{-3} at 2 Pa and 3.5×10^{13} cm^{-3} at 10 Pa. Noticeably, the angular split observed in the density distribution at 20° which starts at 10^{-2} Pa and remains a constant feature for all N_2 pressures. When these results are combined with the XPS data, where no Mn–O–N bonds are visible, the N_2 molecules are likely physically adsorbed on the surface of the films, hindering any subsequent oxidation of the films during deposition.

More information about the plasmas generated in the two regimes was obtained by implementing the technique from ref. 53 for the calculation of the electron temperature and plasma potential. As shown in Fig. S9 and S10, under low-O_2 conditions, several T_e maxima of 4.5 eV are observed at approximately 200 ns, 4.8 eV in the 2.5–3 μs range, and 4 eV in the 6 μs range. For higher pressures, only the contributions in the μs region are noticeable, with intense peaks at 2 and 6 eV being formed above 2 Pa in the <1 μs region. In the N_2 case, a constant T_e contribution ranging between 2.3 and 5.6 eV in the sub μs region is observed for all pressures, with a maximum in the 10^{-2}–2 Pa region. A noticeable feature in the N_2 case is a splitting of the maxima seen in the μs region below 10^{-2} Pa N_2, followed by confinement of the structures at approximately 5 μs, which remains well defined even under high-pressure conditions. In both the N_2 and O_2 cases, a strong increase in the V_p value is observed at <500 ns: a maximum of 10 V is found for 10^{-2}–10^{-1} Pa of N_2 whereas a maximum of 14 eV is found in the 2–5 Pa O_2 region. Similar to the temperature evolution in the 1–10 μs region, a secondary contribution is observed. In the N_2 case, it ranges between 2.3 and 5 V, with the maximum shifting with increasing pressure from 10^{-4} to 2 Pa from 8 μs to 5 μs. In the case of oxygen in the same temporal region, a maximum of 5.3 eV is observed at 6 μs, which results in a shift toward longer evolution times above 2 Pa of O_2 up to 20 μs. Importantly, the increase in both V_p and T_e in the <500 ns range means that in front of the plasma, charges will have greater separation and thus accelerate along the expansion direction, whereas electrons will scatter due to collisions and thus increase the thermal energy of the plasma. The energetic balance shows that MnO molecular formation (386 kJ mol^{-1} formation enthalpy) in the gas phase can occur at low pressures ($<10^{-3}$ Pa for N_2 and <2 Pa for O_2) in the 2–8 μs region but at high pressures in the <1 μs region. For low pressure, oxidation occurs in the core of the plasma, whereas with increasing O_2 or N_2 pressure, oxidation processes occur at the front of the plasma.

4. Conclusions

The growth of highly oriented manganese oxide thin films was investigated to provide a path toward epitaxial growth on MnO. The process involved the implementation of complex morphological and structural characterization of the thin films while simultaneously monitoring the growth process with electrical probes. The growth in N_2 atmospheres leads to the formation of highly oriented MnO coatings that present compressive in-line stress and contain highly oriented defects, which are induced during growth by the high kinetic energy of the plasma. The presence of defects in the MnO crystalline structure was also confirmed by the shift in the bandgap. The presence of O_2 during deposition unlocks the growth of highly crystalline Mn_3O_4 rotated 45 deg to MgO, with XPS measurements showing the presence of high-BE satellites in the 2p region attributed to the contribution of the MnO bonding state on the surface of Mn_3O_4 due to ambient contamination of the sample. The ability of each atmosphere to promote the growth of two selected oxide phases was shown by both ellipsometry and infrared spectroscopy measurements. The *in situ* monitoring of growth highlights the ion acceleration caused by the use of N_2 compared with O_2 and the formation of a plasma environment that is optimal for the formation of molecular species as well as a strong oxide contribution to growth. Both growth conditions induced highly structured density and angular distributions, with N_2 resulting in narrower ion distributions and higher kinetic energies during deposition. A good correlation was observed between the growth environment and the structural and morphological properties of the coatings, creating a general context for the epitaxial growth of MnO and Mn_3O_4.

Author contributions

S.A. Irimiciuc: conceptualization, formal analysis, writing – original draft, writing – review & editing. S. Chertopalov: methodology, formal analysis, visualization. V. Goian: investigation, data curation, visualization. E. de Prado: investigation, formal analysis, visualization, writing – original draft. Martin Vondráček: investigation, formal analysis, visualization. E. Maresova: investigation, formal analysis, data curation, writing – review & editing. P. Svora: investigation, formal analysis. L. Fekete: investigation, formal analysis. Mariana Klementova: formal analysis, writing – original draft, writing – review & editing. S. Kamba: conceptualization, methodology, writing – review & editing. J. Lancok conceptualization, funding acquisition, supervision, writing – review & editing.

Conflicts of interest

There are no conflicts to declare.

Data availability

The datasets generated and analysed during in this manuscript are available at **https://doi.org/10.57680/asep.0640290**.

Supplementary information (SI) containing details on the structural and morphological properties of the thin films as well as extended plasma characterization. See DOI: **https://doi.org/10.1039/d5tc03142g**.

Acknowledgements

This work has been funded by a grant from the Programme Johannes Amos Comenius under the Ministry of Education, Youth and Sports of the Czech Republic SENDISO project no. CZ.02.01.01/00/22_008/0004596. As set out in the Legal Act, beneficiaries must ensure that the open access to the published version or the final peer-reviewed manuscript accepted for publication is provided immediately after the date of publication *via* a trusted repository under the latest available version of the Creative Commons Attribution International Public Licence (CC BY) or a licence with equivalent rights. For long-text formats, CC BY-NC, CC BY-ND, CC BY-NC-ND or equivalent licenses could be applied. This work was supported by the European Union and the Czech Ministry of Education, Youth and Sports (project: MSCA Fellowships CZ FZU II-CZ.02.01.01/00/22_010/0008124). The CzechNanoLab project LM2023051 funded by MEYS CR is gratefully acknowledged for the financial support of the measurements at the LNSM Research Infrastructure.

References

1 S. B. Harris, A. Biswas, S. J. Yun, K. M. Roccapriore, C. M. Rouleau, A. A. Puretzky, R. K. Vasudevan, D. B. Geohegan and K. Xiao, *Small Methods*, 2024, 2301763.
2 D. B. Geohegan, A. A. Puretzky and K. Xiao, *Nat. Mater.*, 2023, **23**(3), 308.
3 S. B. Harris, Y. C. Lin, A. A. Puretzky, L. Liang, O. Dyck, T. Berlijn, G. Eres, C. M. Rouleau, K. Xiao and D. B. Geohegan, *ACS Nano*, 2023, **17**, 2472.
4 G. Bimashofer, S. Smetaczek, E. Gilardi, C. W. Schneider, A. Limbeck, T. Lippert and J. Stahn, *Appl. Phys. A: Mater. Sci. Process.*, 2021, **127**, 473.
5 M. Bator, C. W. Schneider, T. Lippert and A. Wokaun, *Appl. Surf. Sci.*, 2013, **278**, 47–51.
6 F. K. Mohammed, A. Ramizy, N. M. Ahmed, F. K. Yam, Z. Hassan and K. P. Beh, *Opt. Mater.*, 2024, **153**, 115622.
7 H. Wang, Z. Lin, W. Wang, G. Li and J. Luo, *J. Alloys Compd.*, 2017, **718**, 28–35.
8 W. Yang, W. Wang, Y. Lin, S. Zhou, Y. Liu and G. Li, *Mater. Lett.*, 2015, **160**, 20–23.
9 J. Yu, W. Han, A. A. Suleiman, S. Han, N. Miao and F. C. C. Ling, *Small Methods*, 2024, **8**, 2301282.
10 S.-B. Wen, X. Mao, R. Greif and R. E. Russo, *J. Appl. Phys.*, 2007, **101**, 023115.
11 S. K. Yadav and R. K. Singh, *J. Phys. D: Appl. Phys.*, 2020, **101**, 075201.
12 J. Chen, D. Stender, M. Bator, C. W. Schneider, T. Lippert and A. Wokaun, *Appl. Surf. Sci.*, 2013, **278**, 317–320.

13 S. Amoruso, J. Schou, J. G. Lunney and C. Phipps, *AIP Conf. Proc.*, 2010, **1278**, 665–676.
14 E. J. Kautz, M. C. Phillips, A. Zelenyuk and S. S. Harilal, *Phys. Plasmas*, 2022, **29**, 053509.
15 S. S. Harilal, C. M. Murzyn, E. J. Kautz, M. K. Edwards, S. I. Sinkov, S. E. Bisson, S. S. Mitra and J. B. Martin, *J. Anal. At. Spectrom.*, 2021, **36**, 150.
16 S. A. Irimiciuc, S. Chertopalov, J. Lancok and V. Craciun, *Coatings*, 2021, **11**(7), 762.
17 J. Chen, J. G. Lunney, T. Lippert, A. Ojeda-G-P, D. Stender, C. W. Schneider and A. Wokaun, *J. Appl. Phys.*, 2014, **116**, 1.
18 A. Bogaerts, Z. Chen and D. Autrique, *Spectrochim. Acta, Part B*, 2008, **63**, 746.
19 S. A. Irimiciuc, B. C. Hodoroaba, G. Bulai, S. Gurlui and V. Craciun, *Spectrochim. Acta, Part B*, 2020, **165**, 105774.
20 D. Diaz and D. W. Hahn, *Spectrochim. Acta, Part B*, 2020, **166**, 105800.
21 B. D. Ngom, S. Lafane, S. Abdelli-Messaci, T. Kerdja and M. Maaza, *Appl. Phys. A: Mater. Sci. Process.*, 2016, **122**, 1.
22 F. Aubriet, N. Chaoui, R. Chety, B. Maunit, E. Millon and J. F. Muller, *Appl. Surf. Sci.*, 2002, **186**, 282.
23 P. Flanigan and R. Levis, *Annu. Rev. Anal. Chem.*, 2014, **7**, 229.
24 S. A. Irimiciuc, S. Chertopalov, J. Bulíř, M. Vondracek, L. Fekete, P. Jiricek, M. Novotný, V. Craciun and J. Lancok, *Plasma Processes Polym.*, 2022, **19**, 2100102.
25 L. Volfová, S. Andrei Irimiciuc, S. Chertopalov, P. Hruška, J. Čížek, M. Vondráček, M. Novotný, M. Butterling, M. O. Liedke, A. Wagner and J. Lancok, *Appl. Surf. Sci.*, 2023, **608**, 155128.
26 S. A. Irimiciuc, S. Chertopalov, M. Novotný, V. Craciun and J. Lancok, *J. Appl. Phys.*, 2021, **130**, 243302.
27 H. Xia, Y. Wan, F. Yan and L. Lu, *Mater. Chem. Phys.*, 2014, **143**, 720.
28 L. M. Garten, P. Selvarasu, J. Perkins, D. Ginley and A. Zakutayev, *Mater. Adv.*, 2021, **2**, 303.
29 M. Huynh, C. Shi, S. J. L. Billinge and D. G. Nocera, *J. Am. Chem. Soc.*, 2015, **137**, 14887.
30 Q. Xia, S. Sun, J. Xu, F. Zan, J. Yue, Q. Zhang, L. Gu and H. Xia, *Small*, 2018, **14**, 1804149.
31 H. Pan, Y. Shao, P. Yan, Y. Cheng, K. S. Han, Z. Nie, C. Wang, J. Yang, X. Li, P. Bhattacharya, K. T. Mueller and J. Liu, *Nat. Energy*, 2016, **1**, 16039.
32 B. Xu, Y. Bhawe and M. E. Davis, *Proc. Natl. Acad. Sci. U. S. A.*, 2012, **109**, 9260.
33 H. Xia, Y. Wan, F. Yan and L. Lu, *Mater. Chem. Phys.*, 2014, **143**, 720–727.
34 D. Nayak, S. Ghosh and V. Adyam, *Mater. Chem. Phys.*, 2018, **217**, 82–89.
35 M. Putkonen, T. Sajavaara and L. Niinisto, *J. Mater. Chem.*, 2000, **10**, 1857–1861.
36 O. Nilsen, H. Fjellvåg and A. Kjekshus, *Thin Solid Films*, 2003, **444**, 44–51.
37 S. Isber, E. Majdalani, M. Tabbal, T. Christidis, K. Zahraman and B. Nsouli, *Thin Solid Films*, 2009, **517**, 1592–1595.
38 F. Allegretti, C. Franchini, V. Bayer, M. Leitner, G. Parteder, B. Xu, A. Fleming, M. G. Ramsey, R. Podloucky, S. Surnev and F. P. Netzer, *Phys. Rev. B: Condens. Matter Mater. Phys.*, 2007, **75**, 224120.
39 S. A. Irimiciuc, S. Chertopalov, V. Craciun, M. Novotný and J. Lancok, *Plasma Processes Polym.*, 2020, **17**, 2000136.
40 S. A. Irimiciuc, S. Chertopalov, J. Lancok and V. Craciun, *Coatings*, 2021, **11**, 762.
41 A. J. Logsdail, C. A. Downing, T. W. Keal, P. Sherwood, A. A. Sokol and C. R. A. Catlow, *J. Phys. Chem. C*, 2019, **123**, 8133.
42 L. A. Cipriano, G. Di Liberto, S. Tosoni and G. Pacchioni, *J. Chem. Theory Comput.*, 2020, **16**, 3786.
43 E. S. Ilton, J. E. Post, P. J. Heaney, F. T. Ling and S. N. Kerisit, *Appl. Surf. Sci.*, 2016, **366**, 475.
44 J. Petzelt and S. Kamba, *Ferroelectrics*, 2016, **503**, 19–44.
45 A. Kashir, V. Goian, O. Pacherová, M. Savinov, Y. Hee Jeong, G. H. Lee and S. Kamba, *J. Phys.: Condens. Matter*, 2020, **32**, 175402.
46 T. Rudolf, C. Kant, F. Mayr and A. Loidl, *Phys. Rev. B: Condens. Matter Mater. Phys.*, 2008, **77**, 024421.
47 T. Larbi, K. Doll and T. Manoubi, *J. Alloys Compd.*, 2016, **688**, 692–698.
48 S. Amoruso, X. Wang, C. Altucci, C. De Lisio and M. Armenante, *Appl. Phys. Lett.*, 2002, **186**, 358–363.
49 S. S. Harilal, C. V. Bindhu, M. S. Tillack, F. Najmabadi and A. C. Gaeris, *J. Phys. D: Appl. Phys.*, 2002, **35**, 2935–2938.
50 S. A. Irimiciuc, S. Chertopalov, J. Bulíř, L. Fekete, M. Vondráček, M. Novotný, V. Craciun and J. Lancok, *Vacuum*, 2021, **193**, 110528.
51 L. Torrisi and S. Gammino, *Rev. Sci. Instrum.*, 2006, **77**, 1–5.
52 S. Amoruso, I. Unitá, S. Fisiche, N. Federico, M. S. Angelo, V. Cintia, I. Napoli, B. Toftmann and J. Schou, *Phys. Rev. E: Stat., Nonlinear, Soft Matter Phys.*, 2004, **69**, 056403.
53 F. F. Chen, *Phys. Plasmas*, 2001, **8**, 3029–3041.